

Article

Modeling and Control Design of the Symmetrical Interleaved Coupled-Inductor-Based Boost DC-DC Converter with Clamp Circuits

Márcio Rodrigo Santos de Carvalho *, Fabrício Bradaschia, Leonardo Rodrigues Limongi
and Gustavo Medeiros de Souza Azevedo

Department of Electrical Engineering, Federal University of Pernambuco, 50740-550 Recife, Brazil

* Correspondence: mrodrigo.s.c@gmail.com; Tel.: +55-81-98172-0723

Received: 2 August 2019; Accepted: 3 September 2019; Published: 6 September 2019



Abstract: The symmetrical input-interleaved high-gain DC-DC converters are suitable candidates to be used as the first stage in PV microinverters and as parallel-connected power optimizers. In both applications, they are responsible for boosting the PV module DC voltage to a higher value and executing the maximum power point tracking control. However, such converters have many state variables, some of them discontinuous, and many operation stages, which make the development of the small-signal model a challenging task. Therefore, the aim of this paper is to propose a reduced-order improved average method (ROIAM) to model the family member of converters that present characteristics such as symmetry, interleaved operation, and discontinuous state-space variables. ROIAM is applied to model for the first time in the literature the symmetrically-interleaved coupled inductor-based boost (SICIBB), leading to a fourth-order mathematical model (reduced-order model). The complete eighth-order mathematical model is developed as well to prove that the reduced-order model represents correctly the dynamic behavior of the SICIBB converter by employing only four state variables, reducing considerably the effort of the modeling. Based on the reduced-order proposed model, a closed-loop control is designed and tested in a 300-W prototype of the SICIBB converter.

Keywords: discontinuous conduction mode; module integrated converter; small-signal analysis; symmetrical interleaved high-gain DC-DC converter

1. Introduction

In recent years, photovoltaic (PV) energy has grown significantly in terms of installed capacity due to a reduction in PV modules' cost, political regulations establishing feed-in tariffs, technology development, and increased concern about environmental issues [1–3]. Grid-connected PV systems can be classified depending on the PV module arrangement into a centralized inverter, multi-string inverter, string inverter, and AC module [3,4]. The first three ones use PV modules in series to obtain higher DC-link voltage for generating power to AC grid lines [3,4]. However, such configurations have power loss due to PV module mismatch, partial shading, long high voltage DC connection cables, etc. [3,4].

In the AC module system, these drawbacks are mitigated since a low-power (200–300 W) grid-connected inverter, called the PV microinverter (MIC), is mounted in a single PV module, which has its own maximum power point tracking (MPPT), improving, thus, the energy harvesting of the PV system [3,4]. Such capability, known as distributed MPPT, is also addressed in centralized and inverter topologies by employing one DC-DC converter for each PV module. These DC-DC converters, called power optimizers, are connected in series to feed a DC-AC inverter [5].

PV microinverters have the features of lower installation costs, “plug and play” operation, enhanced flexibility and modularity, improved safety, etc. [3]. Due to these advantages, PV microinverters are useful for residential applications with continuous partial shading and complex roof structures with different tilts and orientations [1]. MICs can be classified as single-stage or two-stage conversion systems [1,6]. Single-stage MICs convert the PV module DC voltage (around 22–45 V) directly to AC, while two-stage MICs have a DC-DC stage, responsible for boosting the PV module DC voltage to a higher value (around 200–400 V) and executing the MPPT control and a DC-AC stage that performs the DC-link voltage regulation and the grid-tied functions, which should satisfy the grid standards and codes [1,4,7]. Single-stage MICs usually have higher power density and efficiency when compared with two-stage MICs [7]. However, single-stage MICs use bulky input electrolytic capacitors in order to reduce the double-frequency ripple, which affects the MPPT operation, while reducing the life span of the entire system [6]. On the other hand, the power decoupling in two-stage MICs occurs between stages, using an electrolytic capacitor with reduced volume and proper control strategies in both stages that eliminate the double-frequency ripple influence on the MPPT [6]. The increased life span and the simple/decoupled control system make two-stage MICs more attractive for industrial PV applications [6].

Since both the rated voltage and efficiency of a PV module are very low, high-gain high-efficiency DC-DC converters are required in microinverters and parallel-connected power optimizers to track the maximum available power from a PV module and to boost the DC-link voltage above the minimum value necessary for delivering the generated energy in a 127-V or 220-V single-phase grid [8]. Isolated DC-DC converters such as flyback can achieve high voltage gain by increasing the secondary turns of a high-frequency transformer [8]. However, the use of a transformer results in higher cost and additional losses, reducing the system’s efficiency [8]. In applications where galvanic isolation is not mandatory, transformerless DC-DC converter can operate with high switching frequencies to achieve voltage step-up with lower weight, volume, and cost [8].

Many transformerless DC-DC converters have been proposed to obtain high voltage gain and improved conversion efficiency. Switched capacitor-based converters can achieve high voltage gain by charging the capacitors in parallel and discharging them in series [9]. However, their structure becomes quite complex when the conversion ratio is increased further [8,10]. The conventional series resonant DC-DC converter offers the advantage of high efficiency as it can operate with zero-voltage switching [1]. However, it is not able to regulate a wide input voltage range with a fixed-frequency phase-shift control [11]. Coupled inductor-based DC-DC converters with a clamp circuit have some features such as high voltage gain, high efficiency, leakage inductor energy recycling, and low voltage stress on the switches. Furthermore, the reverse recovery losses of the diodes is reduced due to the leakage inductance of the coupled inductor [12]. Such boosting techniques have also been applied in the impedance source network to offer an efficient means of converting power with a wide range of input voltage regulation [13]: the paper in [14] presented a non-isolated high step-up Z-source DC-DC converter with zero voltage transition operation that combined coupled inductor and switched capacitors; the converter proposed in [15] contained a quasi-active switched-inductor network made up of two coupled inductors. Beyond providing high voltage conversion gain, these DC-DC converters present low voltage stress and low conduction loss on switches, as well as small volume, as they share a single magnetic core. These converters have the main drawback of high input current ripple, which affects the MPPT operation of the PV module [16].

In order to reduce both the input current ripple and the current stress on the switches, the interleaved technique is widely used in step-up DC-DC converters for PV systems [17–21]. Although such DC-DC converters offer high voltage gain, high efficiency, and reduced input current ripple, characteristics very attractive in PV applications, they have a large number of state variables (inductors and capacitors), many operation stages, some of them with time intervals given in terms of the average values of the states variables, and the coexistence of continuous and discontinuous state variables. Thus, the development of the small-signal model and hence the design of the closed-loop

controller of the input voltage necessary to track the maximum power point of the PV module is not straightforward.

In [22], the interleaved boost series resonant converter was modeled through the extended describing functions methodology due to its strongly oscillatory nature. This method gives a continuous-time small-signal model, which can incorporate any number of harmonics to improve model accuracy. In [21], a three-phase interleaved boost converter was modeled, and a proposed switched linear control was implemented on it. In [23,24], dynamic models of the two-phase and six-phase interleaved boost converter were presented, respectively. In [25], a reduced-order model for the boost converter with a voltage multiplier cell was developed by neglecting the resonant energy exchange between the capacitors and assuming a small ripple in the state variables. In such converters, the time intervals of the operation stages are given only in terms of the duty cycle, and all state variables are continuous quantities. Hence, their dynamic behavior is modeled through the conventional state-space averaging modeling approach. In [26], an improved average method (IAM) was proposed to model the asymmetrical interleaved DC-DC converter family operating in discontinuous current conduction mode.

Thus, this paper proposes a reduced-order improved average method (ROIAM) for modeling typical high-gain DC-DC converters that present characteristics such as symmetry, interleaved operation, and discontinuous state-space variables. The proposed method is used to model, for the first time in the literature, the symmetrical interleaved coupled-inductor-based boost (SICIBB) converter with a clamp circuit proposed in [20]. The SICIBB converter presents the main characteristics necessary for the application of the ROIAM: four state-space variables are symmetric to the other four; the currents of the leakage inductances are discontinuous, and the converter presents interleaved operation at its input. The complete-order and reduced-order models of the SICIBB are presented in order to prove that the reduced-order model represents correctly the dynamics of the converter. Both mathematical models and the simulated circuit are verified and compared by simulations. Based on the small-signal reduced-order model, a closed-loop controller is designed and tested in a 300-W prototype of the SICIBB converter. A perturb and observe (P&O) MPPT method is implemented along with the designed control system in order to prove the effectiveness of the proposed method and to show the capability of the SICIBB converter to operate at the maximum power point for different irradiance and temperature conditions.

2. The SICIBB DC-DC Converter

The SICIBB converter topology is composed of two basic coupled inductor-based boost modules, the inputs of which are connected in parallel, generating an interleaved input current, and the output capacitors are associated in series with the input capacitor. In order to avoid interrupting the leakage currents of the coupled inductors, two passive clamp circuits should also be considered. Figure 1 shows the SICIBB converter, which could be a solar optimizer or used as the first stage of an MIC, where:

- L_{m1} and L_{m2} are the magnetizing inductances;
- l_{k1} and l_{k2} are the leakage inductances;
- r_1 and r_2 are the winding resistances;
- $n_1 = \frac{N_{s1}}{N_{p1}}$ and $n_2 = \frac{N_{s2}}{N_{p2}}$ are the turn ratios of the coupled inductors;
- C_1 and C_2 are the output capacitors;
- S_1 and S_2 are the switches;
- $D_{out,1}$ and $D_{out,2}$ are the output diodes;
- C_{c1} and C_{c2} are the clamp capacitors;
- D_{c1} and D_{c2} are the clamp diodes;
- C_{pv} is the input capacitor;
- v_{in} is the input voltage;
- V_0 is the DC-link voltage.

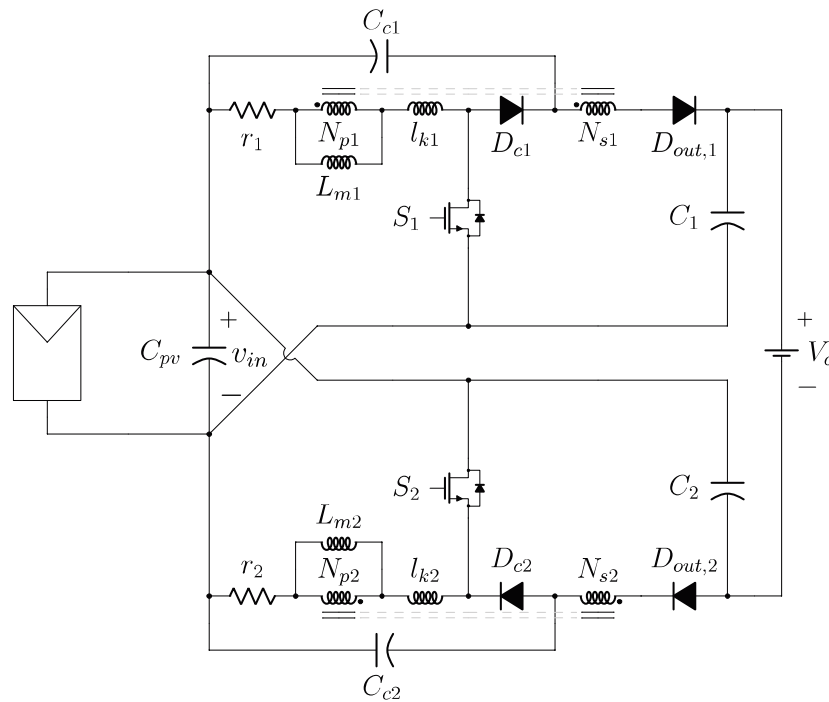


Figure 1. Symmetrical interleaved coupled-inductor-based boost converter.

Assuming that the semiconductors and the coupled inductors are ideal, the two modules are identical, i.e., $L_{m1} = L_{m2}$, $n_1 = n_2 = n$, $C_1 = C_2$, and $C_{c1} = C_{c2}$, and the voltage across the output capacitors, V_{C1} and V_{C2} , and across the clamp capacitors, $V_{C_{c1}}$ and $V_{C_{c2}}$, are constant, the static gain is given by [20]:

$$G = \frac{V_o}{v_{in}} = \frac{1 + D(2n + 1)}{1 - D}. \tag{1}$$

The switches of both boost modules are controlled by gate pulses with the same duty cycle (for step-up operation, consider $D > 0.5$) and 180° phase shift. These conditions impose three combinations on the switches: $(S_1 = on, S_2 = on)$, $(S_1 = off, S_2 = on)$, and $(S_1 = on, S_2 = off)$.

The inductance and diode currents' waveforms and the gate pulses of the switches are presented in Figure 2. One can observe that there are six operation stages with long time intervals inside a switching period, T_s , all of them characterized by the conduction states of the diodes. Table 1 presents the equivalent circuit, state equations, and duration corresponding to these six operation stages, where the first index of the state-space variables indicates the upper (1) and lower (2) modules and the second index identifies the operation stage.

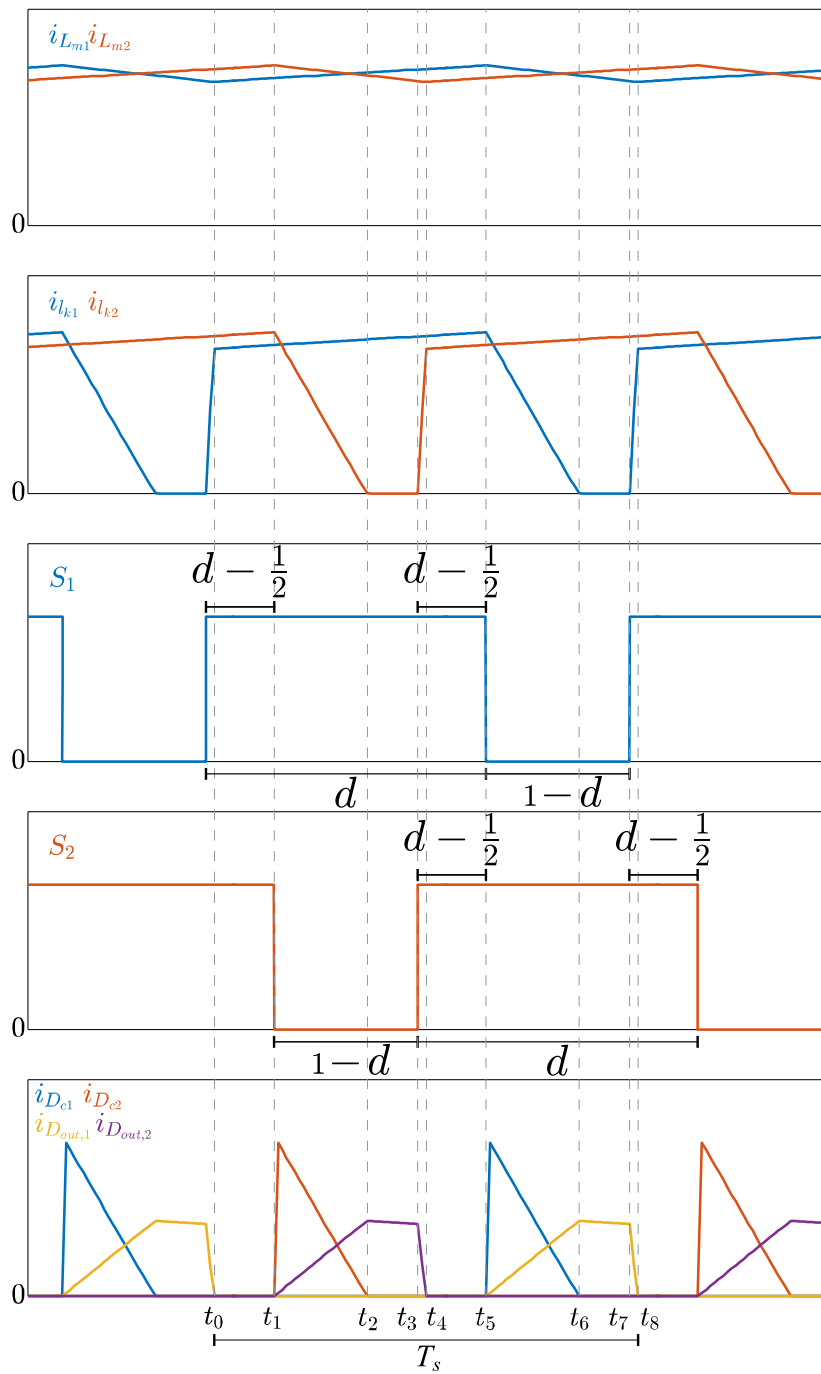


Figure 2. Inductances, diode currents' waveforms, and gate pulses.

Table 1. Operation stages.

Stage	Equivalent Circuit	State-Space Equations	Duration
Stage 1: $[t_0 - t_1], [t_4 - t_5]$		$\dot{i}_{L_{m1,1}} = \frac{-ri_{L_{m1}} + v_{C_1} + v_{C_2} - V_o}{l_k + L_m}$ $\dot{i}_{l_{k1,1}} = \frac{-ri_{L_{m1}} + v_{C_1} + v_{C_2} - V_o}{l_k + L_m}$ $\dot{v}_{C_{1,1}} = \frac{-i_{L_{m1}} - i_{L_{m2}} + i_{pv}}{C + 2C_{pv}}$ $\dot{i}_{L_{m2,1}} = \frac{v_{C_1} - ri_{L_{m2}} + v_{C_2} - V_o}{l_k + L_m}$ $\dot{i}_{l_{k2,1}} = \frac{v_{C_1} - ri_{L_{m2}} + v_{C_2} - V_o}{l_k + L_m}$ $\dot{v}_{C_{2,1}} = \frac{-i_{L_{m1}} - i_{L_{m2}} + i_{pv}}{C + 2C_{pv}}$	
Stage 2: $[t_1 - t_2]$		$\dot{i}_{L_{m1,2}} = \frac{-ri_{L_{m1}} + v_{C_1} + v_{C_2} - V_o}{l_k + L_m}$ $\dot{i}_{l_{k1,2}} = \frac{-ri_{L_{m1}} + v_{C_1} + v_{C_2} - V_o}{l_k + L_m}$ $\dot{v}_{C_{1,2}} = \frac{-Ci_{L_{m1}} - \frac{C+C_{pv}}{n}i_{L_{m2}} + \frac{C+C_{pv}}{n}i_{l_{k2}} + Ci_{pv}}{C^2 + 2C_{pv}C}$ $\dot{i}_{L_{m2,2}} = \frac{v_{C_1} + v_{C_2} - V_o}{L_m n}$ $\dot{i}_{l_{k2,2}} = \frac{-v_{C_1} - nri_{l_{k2}} - (n+1)v_{C_{c2}} + V_o}{l_k n}$ $\dot{v}_{C_{2,2}} = \frac{-Ci_{L_{m1}} + \frac{C_{pv}}{n}i_{L_{m2}} - \frac{C_{pv}}{n}i_{l_{k2}} + Ci_{pv}}{C^2 + 2C_{pv}C}$	

Table 1. Cont.

Stage	Equivalent Circuit	State-Space Equations	Duration
Stage 3: $[t_2 - t_3]$		$i_{L_{m1,3}} = \frac{-ri_{L_{m1}} + v_{C_1} + v_{C_2} - V_o}{l_k + L_m}$ $i_{l_{k1,3}} = \frac{-ri_{L_{m1}} + v_{C_1} + v_{C_2} - V_o}{l_k + L_m}$ $\dot{v}_{C_{1,3}} = \frac{-Ci_{L_{m1}} - \frac{C+C_{pv}}{n}i_{L_{m2}} + Ci_{pv}}{C^2 + 2C_{pv}C}$ $i_{L_{m2,3}} = \frac{v_{C_1} + v_{C_2} - V_o}{L_m n}$ $i_{l_{k2,3}} = 0$ $\dot{v}_{C_{2,3}} = \frac{-Ci_{L_{m1}} + \frac{C_{pv}}{n}i_{L_{m2}} + Ci_{pv}}{C^2 + 2C_{pv}C}$	<p style="text-align: center;">$d_3 \approx 1 - d - d_2$</p>
Stage 4: $[t_5 - t_6]$		$i_{L_{m1,4}} = \frac{v_{C_1} + v_{C_2} - V_o}{L_m n}$ $i_{l_{k1,4}} = \frac{-nri_{l_{k1}} - v_{C_2} - (n+1)v_{C_1} + V_o}{l_k n}$ $\dot{v}_{C_{1,4}} = \frac{\frac{C_{pv}}{n}i_{L_{m1}} - \frac{C_{pv}}{n}i_{l_{k1}} - Ci_{L_{m2}} + Ci_{pv}}{C^2 + 2C_{pv}C}$ $i_{L_{m2,4}} = \frac{v_{C_1} - ri_{L_{m2}} + v_{C_2} - V_o}{l_k + L_m}$ $i_{l_{k2,4}} = \frac{v_{C_1} - ri_{L_{m2}} + v_{C_2} - V_o}{l_k + L_m}$ $\dot{v}_{C_{2,4}} = \frac{-\frac{C+C_{pv}}{n}i_{L_{m1}} + \frac{C+C_{pv}}{n}i_{l_{k1}} - Ci_{L_{m2}} + Ci_{pv}}{C^2 + 2C_{pv}C}$	

Table 1. Cont.

Stage	Equivalent Circuit	State-Space Equations	Duration
Stage 5: $[t_6 - t_7]$		$\dot{i}_{L_{m1,5}} = \frac{v_{C_2} + v_{C_{c1}} - V_o}{L_m n}$ $\dot{i}_{l_{k1,5}} = 0$ $\dot{v}_{C_{1,5}} = \frac{C_{pv}}{n} i_{L_{m1}} - C i_{L_{m2}} + C i_{pv}$ $\dot{i}_{L_{m2,5}} = \frac{v_{C_1} - r i_{L_{m2}} + v_{C_2} - V_o}{l_k + L_m}$ $\dot{i}_{l_{k2,5}} = \frac{v_{C_1} - r i_{L_{m2}} + v_{C_2} - V_o}{l_k + L_m}$ $\dot{v}_{C_{2,5}} = \frac{-\frac{C+C_{pv}}{n} i_{L_{m1}} - C i_{L_{m2}} + C i_{pv}}{C^2 + 2C_{pv}C}$	

It should be noted that the currents through the magnetizing inductances are continuous, while the leakage inductances are discontinuous. Furthermore, for all six operation intervals, $V_o = v_{C_1} + v_{C_2} - v_{in}$.

3. The SICIBB DC-DC Converter Modeling

The dynamic behavior of the SICIBB converter shown in Figure 1 was modeled through the proposed ROIAM. This method consists of obtaining the state equations only for the continuous variables; averaging the state equations, which contain continuous variables of just one module in the conventional way; identifying and including new variables to describe the behavior of the discontinuous variables; obtaining the small-signal model by linearizing the system around a desired operating point; summing the corresponding state variables' coefficients of each module; and representing the system in state-space to obtain the transfer function.

In order to simplify, it was assumed that the semiconductors were ideal; the two modules of the converter were identical; V_o was constant; and the commutation stages (corresponding to the time intervals $[t_3 - t_4]$ and $[t_7 - t_8]$) were neglected. The states variables were the currents through the inductances ($i_{L_{m1}}$, $i_{l_{k1}}$, $i_{L_{m2}}$, and $i_{l_{k2}}$) and the voltages across the capacitors ($v_{C_{c1}}$, v_{C_1} , $v_{C_{c2}}$, and v_{C_2}). The input current, I_{pv} , and the output voltage, V_o , were the input variables. The input voltage (v_{in}) was the output variable.

3.1. Step 1: Calculating d_2 and d_4

The duty cycle corresponding to Stage 2, named d_2 , was obtained by solving the system of equations in (2), formed by the expressions of the voltage across the magnetizing inductance L_{m2} when $S_2 = on$ and the expressions of the average values of the current through the magnetization and leakage inductances, $\langle i_{L_{m2}} \rangle$ and $\langle i_{l_{k2}} \rangle$, yielding (3).

$$\begin{cases} -v_{in} + r\langle i_{L_{m2}} \rangle + (L_m + l_k) \frac{i_{L_{m2,max}} - i_{L_{m2,min}}}{dT_s} = 0 \\ -\langle i_{l_{k2}} \rangle + \frac{i_{L_{m2,min}}d}{2} + \frac{i_{L_{m2,max}}(d + d_2)}{2} = 0 \\ -\langle i_{L_{m2}} \rangle + \frac{i_{L_{m2,max}} + i_{L_{m2,min}}}{2} = 0 \end{cases} \quad (2)$$

$$d_2 = \frac{4(l_k + L_m)(\langle i_{l_{k2}} \rangle - d\langle i_{L_{m2}} \rangle)}{2\langle i_{L_{m2}} \rangle l_k + 2\langle i_{L_{m2}} \rangle L_m + dT_s v_{in} - d\langle i_{L_{m2}} \rangle rT_s} \quad (3)$$

Similarly, the duty cycle corresponding to Stage 4, named d_4 , was obtained by solving the system of equations in (4), formed by the expressions of the voltage across the magnetizing inductance L_{m1} when $S_1 = on$ and the expressions of the average values of the current through the magnetization and leakage inductances, $\langle i_{L_{m1}} \rangle$ and $\langle i_{l_{k1}} \rangle$, yielding (5).

$$\begin{cases} -v_{in} + r\langle i_{L_{m1}} \rangle + (L_m + l_k) \frac{i_{L_{m1,max}} - i_{L_{m1,min}}}{dT_s} = 0 \\ -\langle i_{l_{k1}} \rangle + \frac{i_{L_{m1,min}}d}{2} + \frac{i_{L_{m1,max}}(d + d_4)}{2} = 0 \\ -\langle i_{L_{m1}} \rangle + \frac{i_{L_{m1,max}} + i_{L_{m1,min}}}{2} = 0 \end{cases} \quad (4)$$

$$d_4 = \frac{4(l_k + L_m)(\langle i_{l_{k1}} \rangle - d\langle i_{L_{m1}} \rangle)}{2\langle i_{L_{m1}} \rangle l_k + 2\langle i_{L_{m1}} \rangle L_m + dT_s v_{in} - d\langle i_{L_{m1}} \rangle rT_s} \quad (5)$$

3.2. Step 2: Averaging the State-Space Equations

The averaged equations were calculated by using the conventional method of multiplying each state equation by the corresponding duration and dividing it by the switching period. The result is:

$$\begin{aligned}
 \langle i_{L_{m1}} \rangle &= i_{L_{m1,1}}d_1 + i_{L_{m1,2}}d_2 + i_{L_{m1,3}}d_3 + i_{L_{m1,4}}d_4 + i_{L_{m1,5}}d_5 \\
 \langle i_{l_{k1}} \rangle &= i_{l_{k1,1}}d_1 + i_{l_{k1,2}}d_2 + i_{l_{k1,3}}d_3 + i_{l_{k1,4}}d_4 + i_{l_{k1,5}}d_5 \\
 \langle \dot{v}_{C_1} \rangle &= \dot{v}_{C_{1,1}}d_1 + \dot{v}_{C_{1,2}}d_2 + \dot{v}_{C_{1,3}}d_3 + \dot{v}_{C_{1,4}}d_4 + \dot{v}_{C_{1,5}}d_5 \\
 \langle i_{L_{m2}} \rangle &= i_{L_{m2,1}}d_1 + i_{L_{m2,2}}d_2 + i_{L_{m2,3}}d_3 + i_{L_{m2,4}}d_4 + i_{L_{m2,5}}d_5 \\
 \langle i_{l_{k2}} \rangle &= i_{l_{k2,1}}d_1 + i_{l_{k2,2}}d_2 + i_{l_{k2,3}}d_3 + i_{l_{k2,4}}d_4 + i_{l_{k2,5}}d_5 \\
 \langle \dot{v}_{C_2} \rangle &= \dot{v}_{C_{2,1}}d_1 + \dot{v}_{C_{2,2}}d_2 + \dot{v}_{C_{2,3}}d_3 + \dot{v}_{C_{2,4}}d_4 + \dot{v}_{C_{2,5}}d_5.
 \end{aligned}
 \tag{6}$$

3.3. Step 3: Including the New Variables

As the charging currents of the clamp capacitors were discontinuous, their averaged values were not calculated by averaging the equations as done in Section 3.2. Instead, $\langle \dot{v}_{C_{c1}} \rangle$ and $\langle \dot{v}_{C_{c2}} \rangle$ were given in terms of the currents through the diodes as follows:

$$\begin{aligned}
 C_c \langle \dot{v}_{C_{c1}} \rangle &= \langle i_{D_{c1}} \rangle - \langle i_{D_1} \rangle \\
 C_c \langle \dot{v}_{C_{c2}} \rangle &= \langle i_{D_{c2}} \rangle - \langle i_{D_2} \rangle,
 \end{aligned}
 \tag{7}$$

where:

$$\begin{aligned}
 \langle i_{D_1} \rangle &= \frac{\langle i_{L_{m1}} \rangle - \langle i_{l_{k1}} \rangle}{n} \\
 \langle i_{D_2} \rangle &= \frac{\langle i_{L_{m2}} \rangle - \langle i_{l_{k2}} \rangle}{n}.
 \end{aligned}
 \tag{8}$$

The equations that provided the values of both $\langle i_{l_{k2}} \rangle$ and $\langle i_{L_{m2}} \rangle$ and of both $\langle i_{l_{k1}} \rangle$ and $\langle i_{L_{m1}} \rangle$ were given by Equations (2) and (4), respectively. The average values of the clamp circuit diode currents, $\langle i_{D_{c1}} \rangle$ and $\langle i_{D_{c2}} \rangle$, were the areas of the triangles in the current waveforms shown in Figure 3. The results are:

$$\begin{aligned}
 \langle i_{D_{c1}} \rangle &\simeq \frac{i_{L_{m1,max}}d_2}{2} \\
 \langle i_{D_{c2}} \rangle &\simeq \frac{i_{L_{m2,max}}d_4}{2},
 \end{aligned}
 \tag{9}$$

where the peak currents $i_{L_{m2,max}}$ and $i_{L_{m1,max}}$ were calculated from (2) and (4), respectively, which leads to:

$$\begin{aligned}
 i_{L_{m1,max}} &= \frac{2(l_k + L_m)\langle i_{L_{m1}} \rangle + d_1 T_s \langle v_{in} \rangle + rd_1 T_s \langle i_{L_{m1}} \rangle}{2(l_k + L_m)} \\
 i_{L_{m2,max}} &= \frac{2(l_k + L_m)\langle i_{L_{m2}} \rangle + d_1 T_s \langle v_{in} \rangle + rd_1 T_s \langle i_{L_{m2}} \rangle}{2(l_k + L_m)}.
 \end{aligned}
 \tag{10}$$

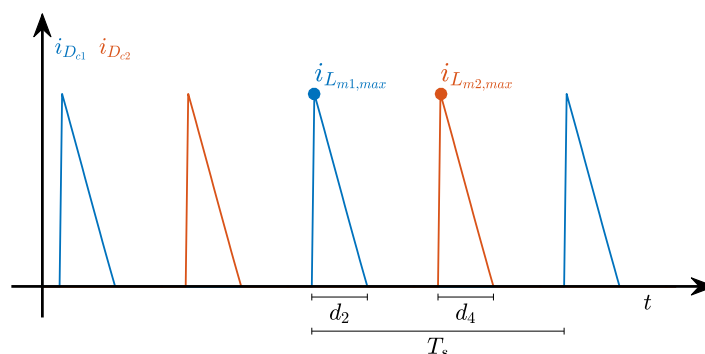


Figure 3. Clamp diodes' currents.

3.4. Step 4: Calculating the Small-Signal AC Models and Transfer Functions' Expressions

To obtain the converter small-signal AC model, Equations (6) and (7) should be linearized around a desired operating point. Let:

$$\langle x \rangle = X + \hat{x} \quad \langle y \rangle = Y + \hat{y} \quad \langle u \rangle = U + \hat{u} \quad d = D + \hat{d},$$

where the uppercase variables define the operation point, the lowercase variables with the hat (^) define small deviations from the operation point, and:

$$x = \begin{bmatrix} i_{L_{m1}} & i_{k1} & v_{C_1} & v_{C_{c1}} & i_{L_{m2}} & i_{k2} & v_{C_2} & v_{C_{c2}} \end{bmatrix}_{1 \times 8}^T$$

$$y = \begin{bmatrix} v_{in} \end{bmatrix}_{1 \times 1}$$

$$u = \begin{bmatrix} i_{pv} & V_o & d \end{bmatrix}_{1 \times 3}^T.$$

Thus, the small-signal linear model is given by:

$$\begin{cases} \hat{x} = A\hat{x} + B\hat{u} \\ \hat{y} = C\hat{x} + E\hat{u} \end{cases} \tag{11}$$

where:

$$A = \begin{bmatrix} \frac{\partial \langle i_{L_{m1}} \rangle}{\partial i_{L_{m1}}} & \frac{\partial \langle i_{L_{m1}} \rangle}{\partial i_{k1}} & \frac{\partial \langle i_{L_{m1}} \rangle}{\partial v_{C_1}} & \frac{\partial \langle i_{L_{m1}} \rangle}{\partial v_{C_{c1}}} & \frac{\partial \langle i_{L_{m1}} \rangle}{\partial i_{L_{m2}}} & \frac{\partial \langle i_{L_{m1}} \rangle}{\partial i_{k2}} & \frac{\partial \langle i_{L_{m1}} \rangle}{\partial v_{C_2}} & \frac{\partial \langle i_{L_{m1}} \rangle}{\partial v_{C_{c2}}} \\ \frac{\partial \langle i_{k1} \rangle}{\partial i_{L_{m1}}} & \frac{\partial \langle i_{k1} \rangle}{\partial i_{k1}} & \frac{\partial \langle i_{k1} \rangle}{\partial v_{C_1}} & \frac{\partial \langle i_{k1} \rangle}{\partial v_{C_{c1}}} & \frac{\partial \langle i_{k1} \rangle}{\partial i_{L_{m2}}} & \frac{\partial \langle i_{k1} \rangle}{\partial i_{k2}} & \frac{\partial \langle i_{k1} \rangle}{\partial v_{C_2}} & \frac{\partial \langle i_{k1} \rangle}{\partial v_{C_{c2}}} \\ \frac{\partial \langle v_{C_1} \rangle}{\partial i_{L_{m1}}} & \frac{\partial \langle v_{C_1} \rangle}{\partial i_{k1}} & \frac{\partial \langle v_{C_1} \rangle}{\partial v_{C_1}} & \frac{\partial \langle v_{C_1} \rangle}{\partial v_{C_{c1}}} & \frac{\partial \langle v_{C_1} \rangle}{\partial i_{L_{m2}}} & \frac{\partial \langle v_{C_1} \rangle}{\partial i_{k2}} & \frac{\partial \langle v_{C_1} \rangle}{\partial v_{C_2}} & \frac{\partial \langle v_{C_1} \rangle}{\partial v_{C_{c2}}} \\ \frac{\partial \langle v_{C_{c1}} \rangle}{\partial i_{L_{m1}}} & \frac{\partial \langle v_{C_{c1}} \rangle}{\partial i_{k1}} & \frac{\partial \langle v_{C_{c1}} \rangle}{\partial v_{C_1}} & \frac{\partial \langle v_{C_{c1}} \rangle}{\partial v_{C_{c1}}} & \frac{\partial \langle v_{C_{c1}} \rangle}{\partial i_{L_{m2}}} & \frac{\partial \langle v_{C_{c1}} \rangle}{\partial i_{k2}} & \frac{\partial \langle v_{C_{c1}} \rangle}{\partial v_{C_2}} & \frac{\partial \langle v_{C_{c1}} \rangle}{\partial v_{C_{c2}}} \\ \frac{\partial \langle i_{L_{m2}} \rangle}{\partial i_{L_{m1}}} & \frac{\partial \langle i_{L_{m2}} \rangle}{\partial i_{k1}} & \frac{\partial \langle i_{L_{m2}} \rangle}{\partial v_{C_1}} & \frac{\partial \langle i_{L_{m2}} \rangle}{\partial v_{C_{c1}}} & \frac{\partial \langle i_{L_{m2}} \rangle}{\partial i_{L_{m2}}} & \frac{\partial \langle i_{L_{m2}} \rangle}{\partial i_{k2}} & \frac{\partial \langle i_{L_{m2}} \rangle}{\partial v_{C_2}} & \frac{\partial \langle i_{L_{m2}} \rangle}{\partial v_{C_{c2}}} \\ \frac{\partial \langle i_{k2} \rangle}{\partial i_{L_{m1}}} & \frac{\partial \langle i_{k2} \rangle}{\partial i_{k1}} & \frac{\partial \langle i_{k2} \rangle}{\partial v_{C_1}} & \frac{\partial \langle i_{k2} \rangle}{\partial v_{C_{c1}}} & \frac{\partial \langle i_{k2} \rangle}{\partial i_{L_{m2}}} & \frac{\partial \langle i_{k2} \rangle}{\partial i_{k2}} & \frac{\partial \langle i_{k2} \rangle}{\partial v_{C_2}} & \frac{\partial \langle i_{k2} \rangle}{\partial v_{C_{c2}}} \\ \frac{\partial \langle v_{C_2} \rangle}{\partial i_{L_{m1}}} & \frac{\partial \langle v_{C_2} \rangle}{\partial i_{k1}} & \frac{\partial \langle v_{C_2} \rangle}{\partial v_{C_1}} & \frac{\partial \langle v_{C_2} \rangle}{\partial v_{C_{c1}}} & \frac{\partial \langle v_{C_2} \rangle}{\partial i_{L_{m2}}} & \frac{\partial \langle v_{C_2} \rangle}{\partial i_{k2}} & \frac{\partial \langle v_{C_2} \rangle}{\partial v_{C_2}} & \frac{\partial \langle v_{C_2} \rangle}{\partial v_{C_{c2}}} \\ \frac{\partial \langle v_{C_{c2}} \rangle}{\partial i_{L_{m1}}} & \frac{\partial \langle v_{C_{c2}} \rangle}{\partial i_{k1}} & \frac{\partial \langle v_{C_{c2}} \rangle}{\partial v_{C_1}} & \frac{\partial \langle v_{C_{c2}} \rangle}{\partial v_{C_{c1}}} & \frac{\partial \langle v_{C_{c2}} \rangle}{\partial i_{L_{m2}}} & \frac{\partial \langle v_{C_{c2}} \rangle}{\partial i_{k2}} & \frac{\partial \langle v_{C_{c2}} \rangle}{\partial v_{C_2}} & \frac{\partial \langle v_{C_{c2}} \rangle}{\partial v_{C_{c2}}} \end{bmatrix}_{8 \times 8} \tag{12}$$

$$B = \begin{bmatrix} \frac{\partial \langle i_{L_{m1}} \rangle}{\partial i_{pv}} & \frac{\partial \langle i_{L_{m1}} \rangle}{\partial V_o} & \frac{\partial \langle i_{L_{m1}} \rangle}{\partial d} \\ \frac{\partial \langle i_{k1} \rangle}{\partial i_{pv}} & \frac{\partial \langle i_{k1} \rangle}{\partial V_o} & \frac{\partial \langle i_{k1} \rangle}{\partial d} \\ \frac{\partial \langle v_{C_1} \rangle}{\partial i_{pv}} & \frac{\partial \langle v_{C_1} \rangle}{\partial V_o} & \frac{\partial \langle v_{C_1} \rangle}{\partial d} \\ \frac{\partial \langle v_{C_{c1}} \rangle}{\partial i_{pv}} & \frac{\partial \langle v_{C_{c1}} \rangle}{\partial V_o} & \frac{\partial \langle v_{C_{c1}} \rangle}{\partial d} \\ \frac{\partial \langle i_{L_{m2}} \rangle}{\partial i_{pv}} & \frac{\partial \langle i_{L_{m2}} \rangle}{\partial V_o} & \frac{\partial \langle i_{L_{m2}} \rangle}{\partial d} \\ \frac{\partial \langle i_{k2} \rangle}{\partial i_{pv}} & \frac{\partial \langle i_{k2} \rangle}{\partial V_o} & \frac{\partial \langle i_{k2} \rangle}{\partial d} \\ \frac{\partial \langle v_{C_2} \rangle}{\partial i_{pv}} & \frac{\partial \langle v_{C_2} \rangle}{\partial V_o} & \frac{\partial \langle v_{C_2} \rangle}{\partial d} \\ \frac{\partial \langle v_{C_{c2}} \rangle}{\partial i_{pv}} & \frac{\partial \langle v_{C_{c2}} \rangle}{\partial V_o} & \frac{\partial \langle v_{C_{c2}} \rangle}{\partial d} \end{bmatrix}_{8 \times 3} \tag{13}$$

$$C = \begin{bmatrix} 0 & 0 & 1 & 0 & 0 & 0 & 1 & 0 \end{bmatrix}_{1 \times 8}$$

$$E = \begin{bmatrix} 0 & -1 & 0 \end{bmatrix}_{1 \times 3}.$$

It is important to observe that, due to the symmetric structure of the converter and the condition of both switches being controlled by the same duty cycle, the corresponding state variables of the boost modules have the same averaged value in a switching cycle, i.e., $\langle i_{Lm1} \rangle = \langle i_{Lm2} \rangle$, $\langle i_{lk1} \rangle = \langle i_{lk2} \rangle$, $\langle v_{C1} \rangle = \langle v_{C2} \rangle$, and $\langle v_{C_{c1}} \rangle = \langle v_{C_{c2}} \rangle$, and the mathematical model of the symmetrical interleaved converter can be derived by using just one module, reducing the order of the model from eight to four.

Taking the upper module into account, the state vector can be redefined as $x_{red} = [i_{Lm} \ i_{lk} \ v_C \ v_{C_c}]_{1 \times 4}^T$. Thus, the state, input, and output matrices are reduced in two steps: (1) the last four lines of the matrices are disregarded, since they are the mirrored version of the first four lines; (2) the last four columns of $A_{8 \times 8}$ and $C_{1 \times 8}$ are added to the first four columns (e.g., Column 1 + Column 5; Column 2 + Column 6...), reducing the number of columns in half, yielding matrices A_{red} , B_{red} , and C_{red} .

$$A_{red} = \begin{bmatrix} \frac{\partial \langle i_{Lm1} \rangle}{\partial i_{Lm1}} + \frac{\partial \langle i_{Lm1} \rangle}{\partial i_{Lm2}} & \frac{\partial \langle i_{Lm1} \rangle}{\partial i_{lk1}} + \frac{\partial \langle i_{Lm1} \rangle}{\partial i_{lk2}} & \frac{\partial \langle i_{Lm1} \rangle}{\partial v_{C1}} + \frac{\partial \langle i_{Lm1} \rangle}{\partial v_{C2}} & \frac{\partial \langle i_{Lm1} \rangle}{\partial v_{C_{c1}}} + \frac{\partial \langle i_{Lm1} \rangle}{\partial v_{C_{c2}}} \\ \frac{\partial \langle i_{lk1} \rangle}{\partial i_{Lm1}} + \frac{\partial \langle i_{lk1} \rangle}{\partial i_{Lm2}} & \frac{\partial \langle i_{lk1} \rangle}{\partial i_{lk1}} + \frac{\partial \langle i_{lk1} \rangle}{\partial i_{lk2}} & \frac{\partial \langle i_{lk1} \rangle}{\partial v_{C1}} + \frac{\partial \langle i_{lk1} \rangle}{\partial v_{C2}} & \frac{\partial \langle i_{lk1} \rangle}{\partial v_{C_{c1}}} + \frac{\partial \langle i_{lk1} \rangle}{\partial v_{C_{c2}}} \\ \frac{\partial \langle v_{C1} \rangle}{\partial i_{Lm1}} + \frac{\partial \langle v_{C1} \rangle}{\partial i_{Lm2}} & \frac{\partial \langle v_{C1} \rangle}{\partial i_{lk1}} + \frac{\partial \langle v_{C1} \rangle}{\partial i_{lk2}} & \frac{\partial \langle v_{C1} \rangle}{\partial v_{C1}} + \frac{\partial \langle v_{C1} \rangle}{\partial v_{C2}} & \frac{\partial \langle v_{C1} \rangle}{\partial v_{C_{c1}}} + \frac{\partial \langle v_{C1} \rangle}{\partial v_{C_{c2}}} \\ \frac{\partial \langle v_{C_{c1}} \rangle}{\partial i_{Lm1}} + \frac{\partial \langle v_{C_{c1}} \rangle}{\partial i_{Lm2}} & \frac{\partial \langle v_{C_{c1}} \rangle}{\partial i_{lk1}} + \frac{\partial \langle v_{C_{c1}} \rangle}{\partial i_{lk2}} & \frac{\partial \langle v_{C_{c1}} \rangle}{\partial v_{C1}} + \frac{\partial \langle v_{C_{c1}} \rangle}{\partial v_{C2}} & \frac{\partial \langle v_{C_{c1}} \rangle}{\partial v_{C_{c1}}} + \frac{\partial \langle v_{C_{c1}} \rangle}{\partial v_{C_{c2}}} \end{bmatrix}_{4 \times 4} \quad (14)$$

$$B_{red} = \begin{bmatrix} \frac{\partial \langle i_{Lm1} \rangle}{\partial i_{pv}} & \frac{\partial \langle i_{Lm1} \rangle}{\partial V_o} & \frac{\partial \langle i_{Lm1} \rangle}{\partial d} \\ \frac{\partial \langle i_{lk1} \rangle}{\partial i_{pv}} & \frac{\partial \langle i_{lk1} \rangle}{\partial V_o} & \frac{\partial \langle i_{lk1} \rangle}{\partial d} \\ \frac{\partial \langle v_{C1} \rangle}{\partial i_{pv}} & \frac{\partial \langle v_{C1} \rangle}{\partial V_o} & \frac{\partial \langle v_{C1} \rangle}{\partial d} \\ \frac{\partial \langle v_{C_{c1}} \rangle}{\partial i_{pv}} & \frac{\partial \langle v_{C_{c1}} \rangle}{\partial V_o} & \frac{\partial \langle v_{C_{c1}} \rangle}{\partial d} \end{bmatrix}_{4 \times 3} \quad (15)$$

$$C_{red} = \begin{bmatrix} 0 & 0 & 2 & 0 \end{bmatrix}_{1 \times 4}. \quad (16)$$

It should be pointed out that, if this symmetric property is used, none of the equations of the bottom module seen in (6) to (10) are necessary to obtain the small signal reduced-order AC model (the fourth-order model).

Finally, the transfer functions can be formulated from the state-space small-signal AC model presented in (11), which leads to:

$$v_{in}(s) = \begin{bmatrix} G_1(s) & G_2(s) & G_3(s) \end{bmatrix}_{1 \times 3} \times \begin{bmatrix} I_{pv}(s) \\ V_o(s) \\ D(s) \end{bmatrix}_{3 \times 1}. \quad (17)$$

4. Validation of the Fourth- and Eighth-Order Models

In order to verify the two main characteristics of the proposed ROIAM, which are the capability to model discontinuous state variables and to reduce the order of the system by using the symmetric structure property, the SICIBB converter shown in Figure 1 was simulated in PSIM using the parameters

given in Table 2. The resulting steady-state conditions of the main variables (desired operation point) are given in Table 3.

Table 2. Simulation parameters of the symmetrically-interleaved coupled inductor-based boost (SICIBB) converter.

Parameter	Value
Duty cycle, D	0.66
Switching frequency, f_{sw}	100 kHz
Input current, I_{pv}	8 A
Output voltage, V_o	400 V
Turns ratio of the coupled inductors, n	2
Magnetizing inductances, L_{m1} and L_{m2}	350 μ H
Leakage inductances, l_{k1} and l_{k2}	3 μ H
Output capacitors, C_1 and C_2	7.5 μ F
Clamp capacitors, C_{c1} and C_{c2}	10 μ F

Table 3. Steady-state conditions.

Variable	Value
$I_{L_{m1}}$ and $I_{L_{m2}}$	5.63 A
$I_{l_{k1}}$ and $I_{l_{k2}}$	4.31 A
$V_{C_{c1}}$ and $V_{C_{c2}}$	65.97 V
V_{C_1} and V_{C_2}	216.70 V
V_{in}	33.40 V

Duty cycle to input voltage transfer functions obtained using the desired operating point given in Table 3 for the fourth-order and eighth-order dynamic models are given by (18) and (19).

$$G_{3,4^{th}}(s) = \frac{-1.212 \cdot 10^5 s^3 - 7.127 \cdot 10^{10} s^2 - 4.52 \cdot 10^{15} s - 5.546 \cdot 10^{19}}{s^4 + 8.771 \cdot 10^5 s^3 + 1.553 \cdot 10^{10} s^2 + 2.936 \cdot 10^{13} s + 4.179 \cdot 10^{17}} \quad (18)$$

$$G_{3,8^{th}}(s) = \frac{-1.214 \cdot 10^5 s^7 - 1.78 \cdot 10^{11} s^6 - 6.903 \cdot 10^{16} s^5 - 5.38 \cdot 10^{21} s^4 - 1.36 \cdot 10^{26} s^3 - 1.116 \cdot 10^{30} s^2 - 8.191 \cdot 10^{32} s - 3.018 \cdot 10^{36}}{s^8 + 1.753 \cdot 10^6 s^7 + 8.031 \cdot 10^{11} s^6 + 3.043 \cdot 10^{16} s^5 + 3.336 \cdot 10^{20} s^4 + 1.135 \cdot 10^{24} s^3 + 9.173 \cdot 10^{27} s^2 + 5.909 \cdot 10^{30} s + 2.273 \cdot 10^{34}} \quad (19)$$

The frequency response of both dynamic models were compared with that obtained from the PSIM AC Sweep tool to verify its correctness. The results are shown in Figure 4.

One can see from the Bode diagrams that the frequency response of both transfer functions and PSIM AC Sweep simulation matched perfectly, except around the resonant frequency, where the peaks' magnitudes from small-signal models were a little higher than that of PSIM AC Sweep. Moreover, there was no difference between the eighth- and fourth-order models. Such results put into evidence the satisfactory prediction of the dynamic behavior of the SICIBB converter provided by both mathematical models, which makes ROIAM a useful method to model directly the converter with only four state variables, reducing considerably the effort of the modeling.

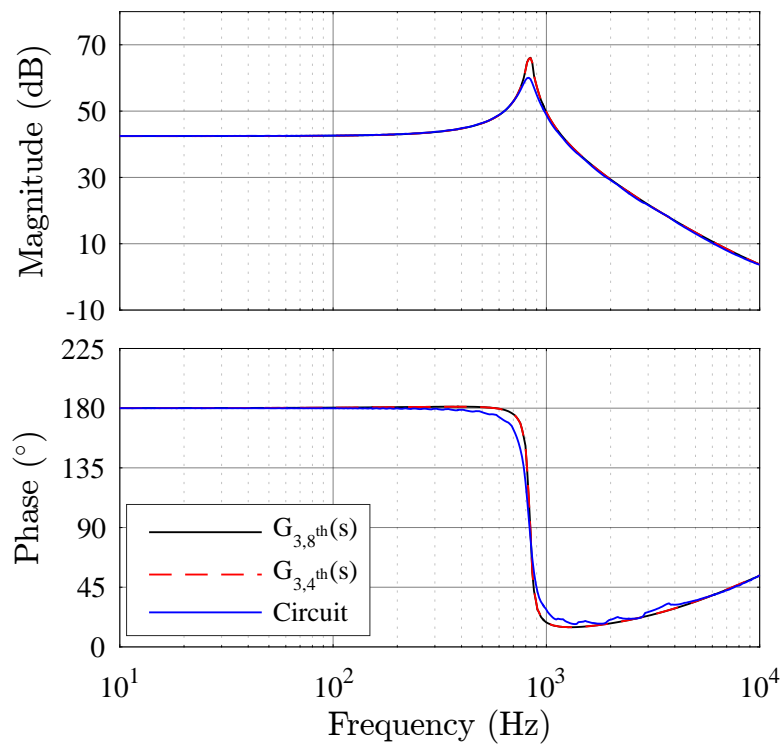


Figure 4. Bode diagram of the duty cycle to input voltage transfer function for the SICIBB converter.

5. Controller Design

Through the dynamic model obtained in Section 3, the controller was designed for compensation of the error between the output and the reference. From (17), the input voltage (v_{in}) of the DC-DC converter depended on the input current (I_{pv}), the output voltage (V_o), and the duty cycle (D). In two-stage MICs and solar power optimizers, I_{pv} changes slowly at a rate defined by the MPPT, and V_o is controlled by the inverter stage. Hence, variations in I_{pv} and V_o were considered output disturbances, v_{in} being controlled exclusively by D . Therefore, only $G_3(s)$ was required to design the input voltage controller; for simplicity, $G_{3,4th}(s)$ was chosen. Figure 5 shows the block diagram of the input voltage control scheme.

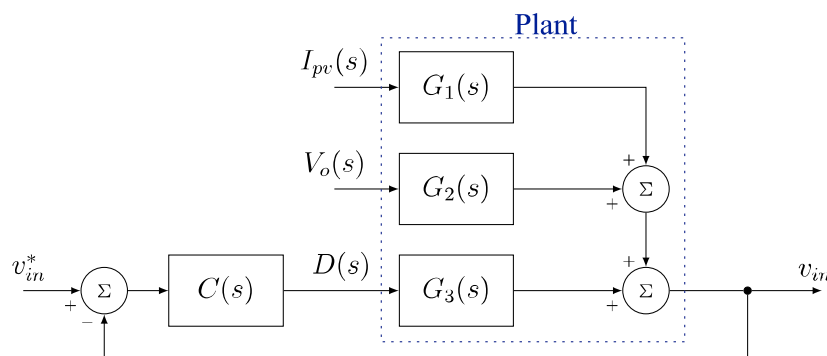


Figure 5. Block diagram of the input voltage control scheme.

Aiming to reject output disturbances and to track the input voltage reference quickly, a 0-dB crossover frequency around 10 kHz and a phase margin around 20° were chosen. The controller that is able to meet such requirements is a proportional-integral (PI) controller plus lead compensator. In the continuous w -domain, the transfer function of the designed controller is given by:

$$C(w) = -0.72 \times \frac{(w + 62.8)}{w} \times \frac{(w + 4.18 \times 10^4)}{(w + 7.64 \times 10^4)}. \quad (20)$$

The frequency response of the input voltage control is shown in Figure 6, including the open-loop transfer function ($G_{3,4th}(w)$), controller transfer function ($C(w)$), and compensated loop transfer function ($C(w)G_{3,4th}(w)$). The gain margin (G_m) and phase margin (P_m) of the compensated DC-DC converter were $G_m = 4.71$ dB and $P_m = 20.1^\circ$, as shown in Figure 6.

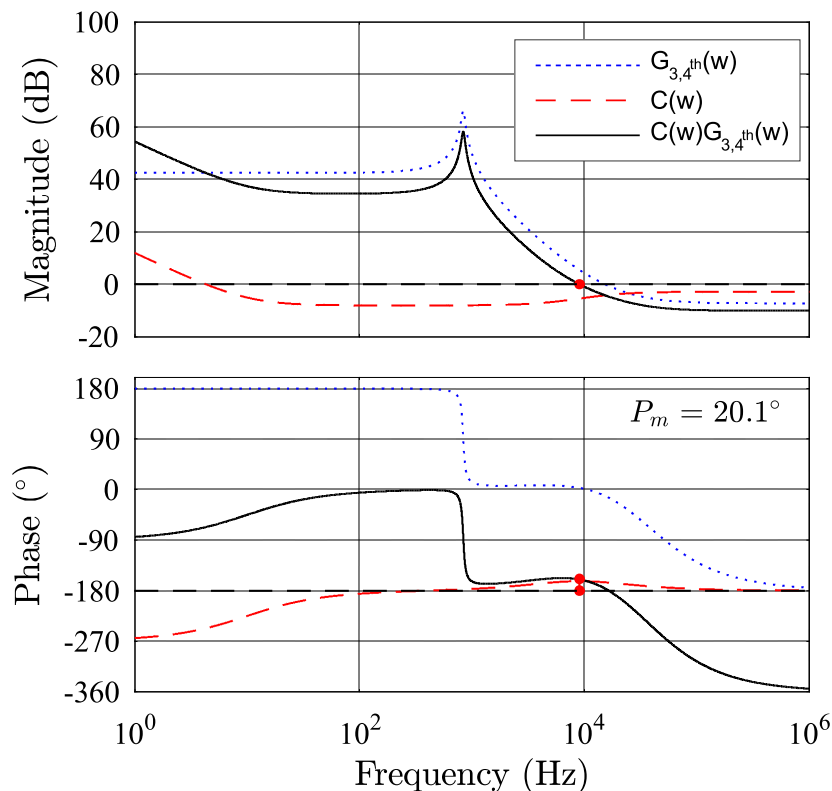


Figure 6. Controller design Bode diagram in the w -domain.

In order to implement the controller in a digital signal processor (DSP), $C(w)$ given by (20) was discretized by the Tustin method. After a partial fraction expansion process, the result can be expressed in terms of the proportional gain (K_p) and the integral gain (k_i) as follows:

$$C(z) = k_p + \frac{k_i T_s}{z - 1} + \frac{a}{z - b}, \quad (21)$$

where $k_p = -0.630067$, $a = 0.130327$, $b = 0.447178$, and $k_i T_s = -0.000247$, which implies $k_i = -24.7$, since the switching period is $10 \mu\text{s}$.

6. Experimental Results

In order to validate the previous theoretical and simulation analyses including the small-signal model derived by the proposed ROIAM, a 300-W experimental prototype was built. A picture of the prototype is shown in Figure 7, and the main design specifications are presented in Tables 2 and 4. The component list used in the prototype is presented in Table 5. The control was implemented by the TMS320F28335 DSP, which is capable of generating two gate signals with an adjustable duty cycle and a 180° phase shift. The voltage and the current at the input were measured with transducers AMC 1301 and ACS 722, respectively.

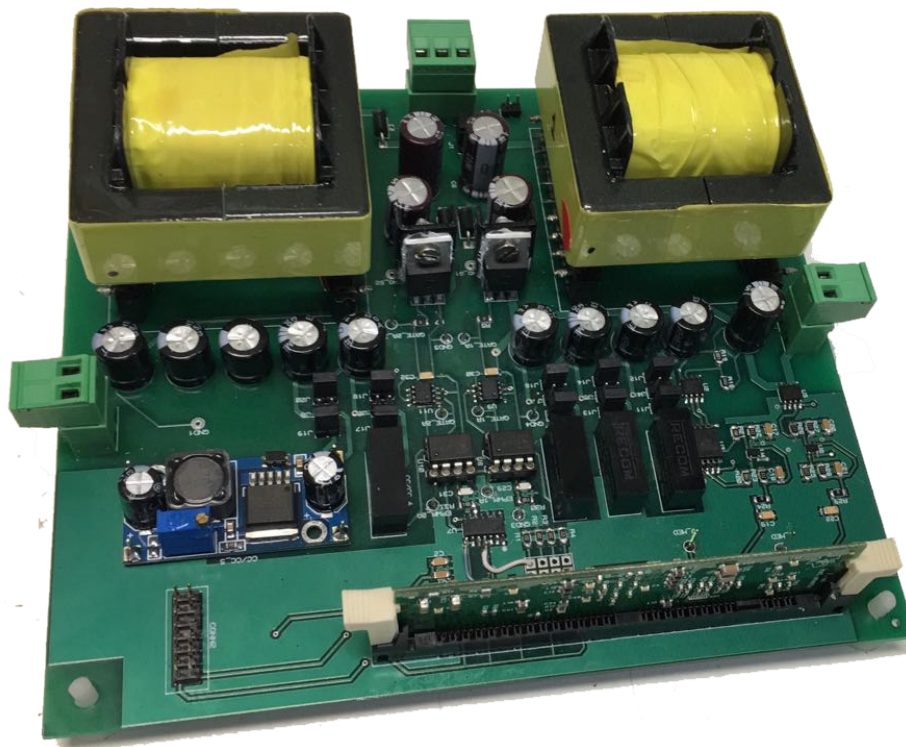


Figure 7. The 300-W prototype of the SICIBB converter.

Table 4. Design specifications.

Parameter	Value
Rated power	300 W
Switching frequency	100 kHz
Input DC voltage	10~40 V
Output voltage	400 V

Table 5. Devices used in the prototype.

Circuit Element	Device
Digital signal processor	TMS320F28335
Voltage sensor	AMC 1301
Current sensor	ACS 722
C_{c1} and C_{c2}	10 μ F, 200 V, electrolytic
C_1 and C_2	10 μ F, 400 V, electrolytic
C_{pv}	100 μ F, 50 V, electrolytic
S_1 and S_2	IPP320N20N3 (MOSFET) 200 V, 34 A
$D_{out,1}$, $D_{out,2}$, D_{c1} , and D_{c2}	STTH3R04 400 V, 3 A
Coupled inductor	350 μ H, NEE-55/28/21 IP12R Thornton, 27/54

According to the waveforms of the SICIBB converter operation shown in Figure 8, the current through the leakage inductance reached zero and remained there for a certain period of time. It should be pointed out that the current through the magnetizing inductance presented in Figure 8 was obtained by $i_{i_{k1}} + 2i_{D1}$. In order to verify the control system design, a step change from 20 V to 35 V in the

reference input voltage was carried out, and the results are shown in Figures 9 and 10. It is possible to note that the input voltage took 35 ms to reach its new reference value.

In order to verify the capability of the SICIBB converter and its control system to find the maximum power point (MPP) of a PV module, the conventional P&O algorithm was implemented in the DSP, and the PV solar array simulator Chroma 62150H-600S was connected at the SICIBB converter's input, emulating the behavior of an 80-W PV module. The P&O algorithm was tested for five different irradiance (S) and temperature (T) conditions, as seen in Table 6. In each case, a different voltage value was associated with the MPP, and the P&O algorithm should be able to track it.

The experimental result can be seen in Figure 11, where a different S and T condition was imposed on the PV module every four seconds. It is possible to see that the SICIBB converter was able to track the MPP in each case, i.e., the control system, designed based on the fourth-order model, was effective.

Table 6. Optimal operating voltage (V_{mp}) and power (P_{mp}) for different irradiances (S) and temperatures (T).

Case	S [$\frac{W}{m^2}$]	T [$^{\circ}C$]	V_{mp} [V]	P_{mp} [W]
1	401	40	15.86	29.16
2	1061	57	14.72	73.64
3	587	22	17.43	47.01
4	288	59	14.40	19.49
5	1125	32	16.85	86.78

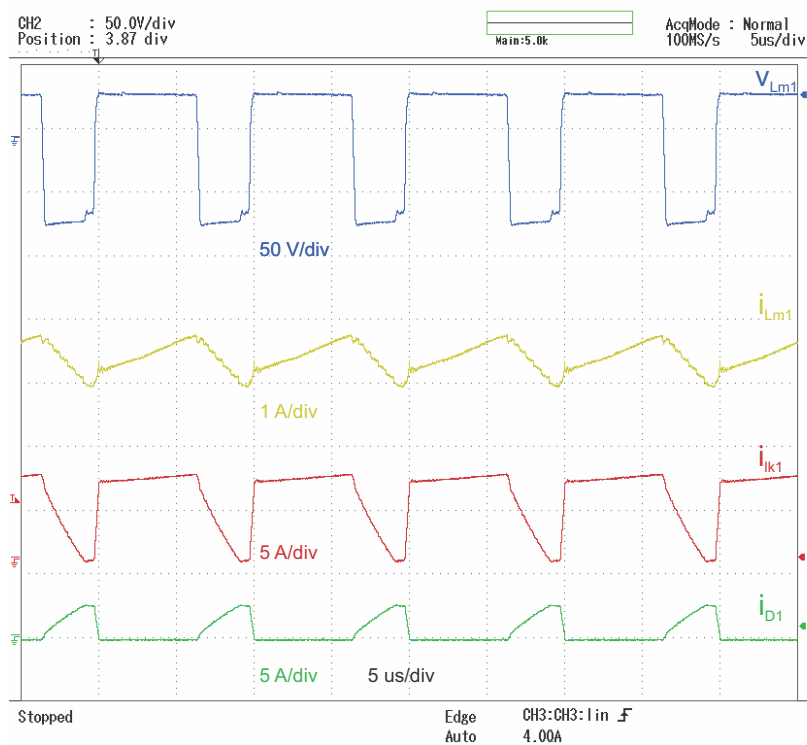


Figure 8. Main experimental waveforms of the SICIBB.

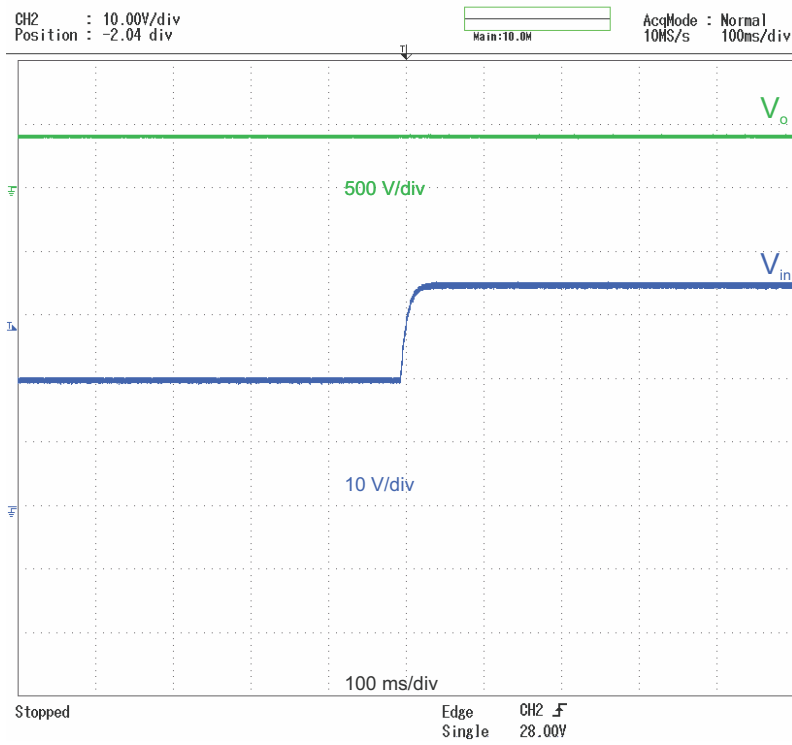


Figure 9. Dynamic response of the input voltage control for a step change from 20 V to 35 V.

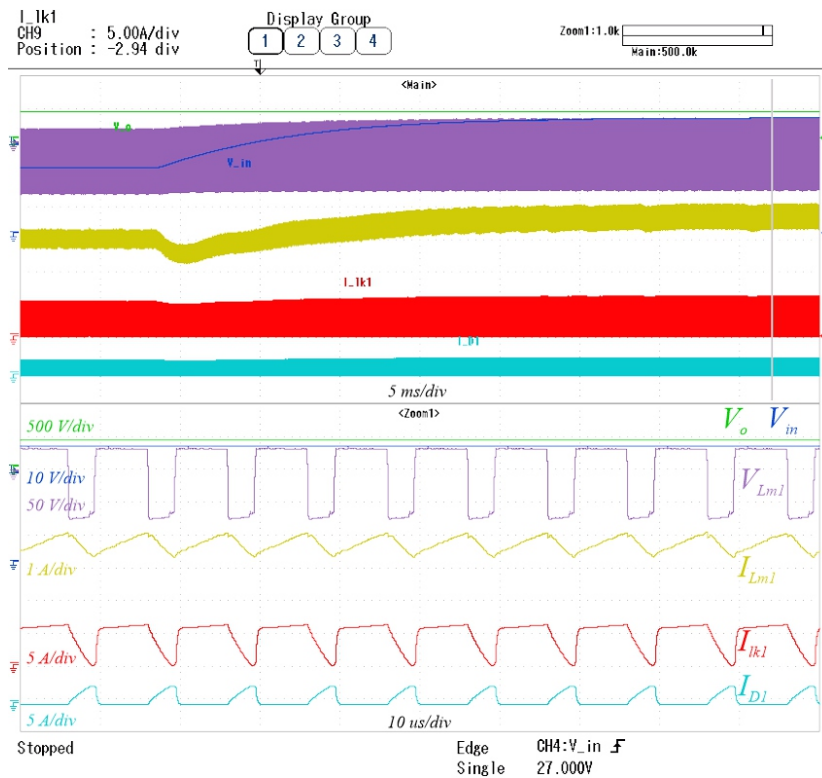


Figure 10. Dynamic response of the main waveforms of the SICIBB converter for a step change from 20 V to 35 V at 8 ms.

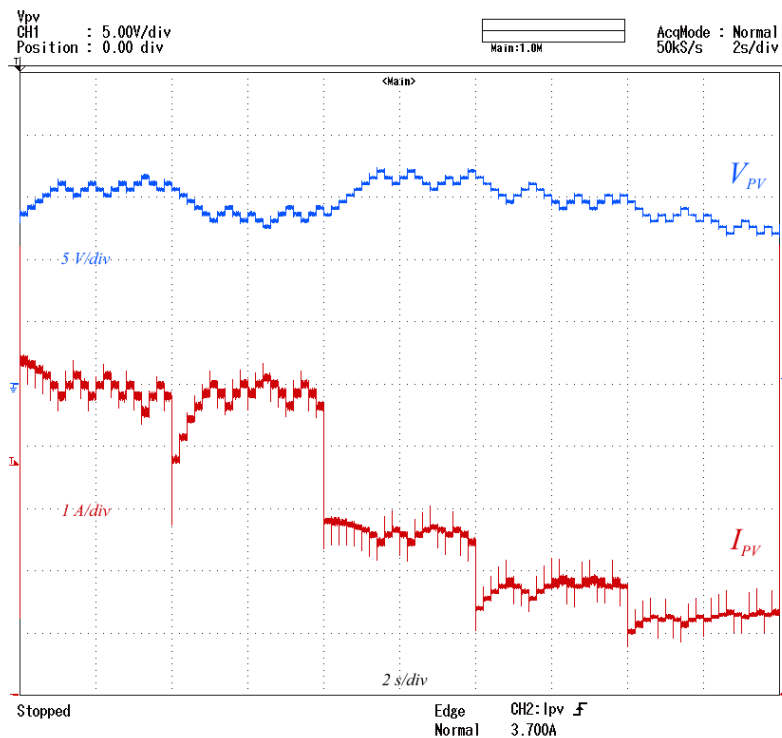


Figure 11. PV module voltage and current (V_{pv} and I_{pv} , respectively) for five different temperature and irradiance conditions, when the P&O algorithm is implemented in the SICIBB converter.

7. Conclusions

This paper proposed a reduced-order improved average method to overcome the challenge of accurately modeling typical high-gain DC-DC converters that present characteristics such as symmetry, input interleaved, a large number of state variables, many operation stages, and the coexistence of continuous and discontinuous state variables.

ROIAM was used to model the SICIBB converter, resulting in a fourth-order mathematical model. By simulation, there was no difference between the frequency response of the fourth-order and the eighth-order models developed in this paper as well. Their frequency responses were compared with the simulated circuit in PSIM, exhibiting a perfect match, except around the resonant frequency. Such simulation results validated the capabilities of the ROIAM to model discontinuous state variables and to reduce the order of the system, reducing the effort of the modeling task.

The satisfactory accuracy in the frequency response of the duty cycle to input voltage fourth-order transfer function provided by the ROIAM made it possible to design a PI controller plus lead compensator for the SICIBB converter. The SICIBB convert and its closed loop control system were verified experimentally through a step change in the reference input voltage and implementing a P&O algorithm to find the maximum power point for five different irradiance and temperature conditions. In both cases, the results proved the effectiveness of the proposed ROIAM applied for the SICIBB converter.

Author Contributions: Conceptualization, M.R.S.C.; Formal analysis, M.R.S.C. and F.B.; Funding acquisition, L.R.L. and G.M.S.A.; Investigation, M.R.S.C., F.B. and L.R.L.; Supervision, F.B., L.R.L. and G.M.S.A.; Validation, M.R.S.C. and F.B.; Writing—original draft, M.R.S.C., F.B. and G.M.S.A.; Writing—review & editing, F.B., L.R.L. and G.M.S.A.

Funding: This work was partially supported by CAPES, CNPq Grant No. 306304/2018-0 and No. 309789/2017-6 and FACEPE Grant No. APQ-0777-3.04/14, No. APQ-0896-3.04/14, No. APQ-0903-3.04/14 and No. IBPG-0935-3.04/18.

Conflicts of Interest: The authors declare no conflict of interest.

References

1. Kouro, S.; Leon, J.I.; Vinnikov, D.; Franquelo, L.G. Grid-Connected Photovoltaic Systems: An Overview of Recent Research and Emerging PV Converter Technology. *IEEE Ind. Electron. Mag.* **2015**, *9*, 47–61. [[CrossRef](#)]
2. Zhang, X.; Zhao, T.; Mao, W.; Tan, D.; Chang, L. Multilevel Inverters for Grid-Connected Photovoltaic Applications: Examining Emerging Trends. *IEEE Power Electron. Mag.* **2018**, *5*, 32–41. [[CrossRef](#)]
3. Zeb, K.; Uddin, W.; Khan, M.A.; Ali, Z.; Ali, M.U.; Christofides, N.; Kim, H.J. A comprehensive review on inverter topologies and control strategies for grid connected photovoltaic system. *Renew. Sustain. Energy Rev.* **2018**, *94*, 1120–1141. [[CrossRef](#)]
4. Anzalchi, A.; Sarwat, A. Overview of technical specifications for grid-connected photovoltaic systems. *Energy Convers. Manag.* **2017**, *152*, 312–327. [[CrossRef](#)]
5. Balato, M.; Vitelli, M. A new control strategy for the optimization of Distributed MPPT in PV applications. *Int. J. Electr. Power Energy Syst.* **2014**, *62*, 763–773. [[CrossRef](#)]
6. Zhao, X.; Zhang, L.; Born, R.; Lai, J. A High-Efficiency Hybrid Resonant Converter With Wide-Input Regulation for Photovoltaic Applications. *IEEE Trans. Ind. Electron.* **2017**, *64*, 3684–3695. [[CrossRef](#)]
7. Xiao, W.; el Moursi, M.S.; Khan, O.; Infield, D. Review of grid-tied converter topologies used in photovoltaic systems. *IET Renew. Power Gener.* **2016**, *10*, 1543–1551. [[CrossRef](#)]
8. Revathi, B.S.; Prabhakar, M. Non isolated high gain DC-DC converter topologies for PV applications—A comprehensive review. *Renew. Sustain. Energy Rev.* **2016**, *66*, 920–933. [[CrossRef](#)]
9. Wu, G.; Ruan, X.; Ye, Z. Nonisolated High Step-up DC-DC Converters Adopting Switched-Capacitor Cell. *IEEE Trans. Ind. Electron.* **2015**, *62*, 383–393. [[CrossRef](#)]
10. Wu, G.; Ruan, X.; Ye, Z. High Step-up DC-DC Converter Based on Switched Capacitor and Coupled Inductor. *IEEE Trans. Ind. Electron.* **2018**, *65*, 5572–5579. [[CrossRef](#)]
11. Shen, Y.; Wang, H.; Shen, Z.; Yang, Y.; Blaabjerg, F. A 1-MHz Series Resonant DC-DC Converter with a Dual-Mode Rectifier for PV Microinverters. *IEEE Trans. Power Electron.* **2019**, *34*, 6544–6564. [[CrossRef](#)]
12. Zhao, Q.; Tao, F.; Lee, F.C. A front-end DC/DC converter for network server applications. In Proceedings of the 2001 IEEE 32nd Annual Power Electronics Specialists Conference (IEEE Cat. No.01CH37230), Vancouver, BC, Canada, 17–21 June 2001; Volume 3, pp. 1535–1539.
13. Liu, H.; Li, F.; Wheeler, P. A Family of DC-DC Converters Deduced From Impedance Source DC-DC Converters for High Step-up Conversion. *IEEE Trans. Ind. Electron.* **2016**, *63*, 6856–6866. [[CrossRef](#)]
14. Poorali, B.; Jazi, H.M.; Adib, E. Improved High Step-up Z-Source DC-DC Converter with Single Core and ZVT Operation. *IEEE Trans. Power Electron.* **2018**, *33*, 9647–9655. [[CrossRef](#)]
15. Liu, H.; Li, F. A Novel High Step-up Converter With a Quasi-active Switched-Inductor Structure for Renewable Energy Systems. *IEEE Trans. Power Electron.* **2016**, *31*, 5030–5039. [[CrossRef](#)]
16. Ardi, H.; Ajami, A.; Sabahi, M. A Novel High Step-up DC-DC Converter with Continuous Input Current Integrating Coupled Inductor for Renewable Energy Applications. *IEEE Trans. Ind. Electron.* **2018**, *65*, 1306–1315. [[CrossRef](#)]
17. Tseng, K.; Chen, J.; Lin, J.; Huang, C.; Yen, T. High Step-up Interleaved Forward-Flyback Boost Converter with Three-Winding Coupled Inductors. *IEEE Trans. Power Electron.* **2015**, *30*, 4696–4703. [[CrossRef](#)]
18. Nouri, T.; Vosoughi, N.; Hosseini, S.H.; Babaei, E.; Sabahi, M. An Interleaved High Step-up Converter with Coupled Inductor and Built-In Transformer Voltage Multiplier Cell Techniques. *IEEE Trans. Ind. Electron.* **2019**, *66*, 1894–1905. [[CrossRef](#)]
19. Tseng, K.; Cheng, C.; Chen, C. High Step-up Interleaved Boost Converter for Distributed Generation Using Renewable and Alternative Power Sources. *IEEE J. Emerg. Sel. Top. Power Electron.* **2017**, *5*, 713–722. [[CrossRef](#)]
20. Kianpour, A.; Jabbari, M.; Shahgholian, G. High step-up floating-output interleaved-input coupled-inductor-based boost converter. In Proceedings of the 2016 24th Iranian Conference on Electrical Engineering (ICEE), Shiraz, Iran, 10–12 May 2016; pp. 1088–1093.
21. Mojallizadeh, M.R.; Badamchizadeh, M.A. Switched linear control of interleaved boost converters. *Int. J. Electr. Power Energy Syst.* **2019**, *109*, 526–534. [[CrossRef](#)]

22. Garcia-Rodriguez, L.A.; Deng, C.; Balda, J.C.; Escobar-Mejia, A. Analysis, modeling and control of an interleaved isolated boost series resonant converter for microinverter applications. In Proceedings of the 2016 IEEE Applied Power Electronics Conference and Exposition (APEC), Long Beach, CA, USA, 20–24 March 2016; pp. 362–369.
23. Garcia, F.S.; Pomilio, J.A.; Spiazzi, G. Modeling and Control Design of the Interleaved Double Dual Boost Converter. *IEEE Trans. Ind. Electron.* **2013**, *60*, 3283–3290. [[CrossRef](#)]
24. Garcia, F.S.; Pomilio, J.A.; Spiazzi, G. Modeling and control design of the six-phase Interleaved Double Dual Boost converter. In Proceedings of the 2010 9th IEEE/IAS International Conference on Industry Applications—INDUSCON 2010, Sao Paulo, Brazil, 8–10 November 2010; pp. 1–6.
25. Dupont, F.H.; Rech, C.; Gules, R.; Pinheiro, J.R. Reduced-Order Model and Control Approach for the Boost Converter with a Voltage Multiplier Cell. *IEEE Trans. Power Electron.* **2013**, *28*, 3395–3404. [[CrossRef](#)]
26. Arango, E.; Ramos-Paja, C.A.; Calvente, J.; Giral, R.; Serna-Garces, S.I. Asymmetrical Interleaved DC-DC Switching Converters for Photovoltaic and Fuel Cell Applications—Part 2: Control-Oriented Models. *Energies* **2013**, *6*, 5570–5596. [[CrossRef](#)]



© 2019 by the authors. Licensee MDPI, Basel, Switzerland. This article is an open access article distributed under the terms and conditions of the Creative Commons Attribution (CC BY) license (<http://creativecommons.org/licenses/by/4.0/>).